Eur. Phys. J. B (2022)95:4
https://doi.org/10.1140/epjb/s10051-021-00269-7

THE EUROPEAN
PHYSICAL JOURNAL B

Regular Article - Statistical and Nonlinear Physics

Influence of sodium inward current on the dynamical behaviour of modified Morris-Lecar model

H. O. Fatoyinbo[1,a], S. S. Muni[1,b], and A. Abidemi[2,c]

[1] School of Fundamental Sciences, Massey University, Palmerston North, New Zealand
[2] Department of Mathematical Sciences, Federal University of Technology, Akure, Nigeria

Received 11 September 2021 / Accepted 17 December 2021

Abstract. This paper presents a modified Morris-Lecar model by incorporating the sodium inward current. The dynamical behaviour of the model in response to key parameters is investigated. The model exhibits various excitability properties as the values of parameters are varied. We have examined the effects of changes in maximum ion conductances and external current on the dynamics of the membrane potential. A detailed numerical bifurcation analysis is conducted. The bifurcation structures obtained in this study are not present in existing bifurcation studies of the original Morris-Lecar model. The results in this study provide the interpretation of electrical activity in excitable cells and a platform for further study.

1 Introduction

The variation in concentration of ions across the cell membrane results in fluxes of ions through the voltage-gated ion channels. This electrophysiological process in the cell membrane plays a fundamental role in understanding the electrical activities in excitable cells such as neurons [33], muscle cells [15] and hormones [21]. The temporal variation of the cell membrane potential due to external stimulation is known as an action potential. Different ion channels play different roles in the generation of an action potential. Depending on the cell, the opening of Na^+ (Ca^{2+}) channels causes influx of Na^+ (Ca^{2+}) and the membrane potential becomes more positive, hence the membrane is depolarised. When the K^+ channels are open, there is efflux of K^+ which results in the repolarisation of the cell. Later, the membrane potential becomes more negative than the resting potential and the membrane is hyperpolarised. At this stage, the membrane will not respond to stimulus until it returns to the resting potential [9,10,22,25].

From the viewpoint of mathematics, numerous mathematical models have been developed to study the nonlinear dynamics involved in the generation of an action potential in the cell membrane. They are often modelled by a nonlinear system of ordinary differential equations (ODEs). Among the famous works is the one by Hodgkin and Huxley [20] on the conduction of electrical impulses along a squid giant axon. In their experiments, it was reported that action potentials depend on the influx of Na^+. This work laid the foundation for other electrophysiological models. Other well-known models are the FitzHugh-Nagumo model [12,36], the Morris-Lecar (ML) model [34], the Chay model [5], and the Smolen and Keizer model [43].

ML model describes the electrical activities of a giant barnacle muscle fibre membrane. Despite being a model for muscle cell, it has been widely used in modelling electrical activities in other excitable cells mostly in neurons [2,23,37,49]. Based on experimental observations, ML model is formulated on the assumption that the electrical activities in barnacle muscle depend largely on fluxes of Ca^{2+} and K^+ rather than Na^+. On this basis, their model consists of three ODEs. It is observed that the Ca^{2+} current activates faster than the K^+ current and the charging capacitor [26]. Thus, the model is further reduced to two ODEs by setting the Ca^{2+} activation to quasi-steady state.

The two-dimensional ML model has been extensively used in many single-cell models [11,30,46,47] and network of cells [13,19,29,32] studies despite it is an approximation of the three-dimensional ML model. In spite of little attention to the three-dimensional model, it has been used in modelling electrophysiological studies. For example, Gottschalk and Haney [17] investigated how the activity of the ion channels are regulated by anaesthetics. The three-dimensional ML model was used by Marreiros et al. [31] for modelling dynamics in neuronal populations using a statistical approach. Also, González-Miranda [16] investigated pacemaker dynamics in ML model using the three-dimensional model. Gall and Zhou [14] considered four-dimensional ML model by including the second inward Na^+ current.

Many recent papers have studied modified ML model by adding relevant inward and outward ionic currents

---

[a] e-mail: h.fatoyinbo@massey.ac.nz (corresponding author)
[b] e-mail: s.muni@massey.ac.nz
[c] e-mail: aabidemi@futa.edu.ng

[1,3,7,32,38]. Zeldenrust et al. [48] extended the ML model by including three additional ionic membrane currents: a T-type calcium current, a cation selective h-current and a calcium-dependent potassium current to investigate reliability of spikes in thalamocortical relay cells. Also, Azizi and Mugabi [2] added calcium-dependent potassium current to the ML model to study bursting properties in neurons. They showed that the model has complex dynamical behaviour including square-wave, elliptic, and parabolic busters depending on parameter combinations. Rajagopal et al. [39] modified the ML model by incoporating the influence of electric and magnetic field on dynamical behaviours of network of neurons. They found complex spatiotemporal dynamics including chaotic bursting and spiral waves.

The purpose of this paper is to investigate the influence of sodium inward currents on the variation of membrane voltage of a single excitable cell. In recent years, experimental and computational analyses have suggested that sodium currents are relevant in the generation of action potential in some muscle cells [4,24,45]. Bifurcation analysis is often used to investigate the mode of the transition of electrical activities of excitable cells. It helps us to identify the key parameters that cause changes in the dynamical behaviour qualitatively [25,28]. A lot of studies on bifurcation analyses have been carried out on the two-dimensional [11,18,38,44] and three-dimensional [16] ML models, however, to our knowledge there appears no work in the literature that has extensively considered the bifurcation analysis of the four-dimensional ML model. In this present paper, we focus on the maximum conductances of ion currents and external current as bifurcation parameters. As a consequence, we show some additional bifurcation that are not present in the existing results of ML model.

The paper is organised as follows. In Sect. 2, we present the model equations and the dynamics of the model upon variation of model parameters. A detailed bifurcation analyses are carried out in Sect. 3. Finally, the conclusion is presented in Sect. 4.

2 Model equation

The classical Morris-Lecar (ML) model [34] is a three-dimensional nonlinear system of ODEs, which is described as

$$\mathrm{C}\frac{dV}{dt} = I_{\mathrm{ext}} - I_{\mathrm{L}} - I_{\mathrm{Ca}} - I_{\mathrm{K}}, \tag{1}$$

$$\frac{dm}{dt} = \lambda_m(V)(m_\infty(V) - m), \tag{2}$$

$$\frac{dn}{dt} = \lambda_n(V)(n_\infty(V) - n), \tag{3}$$

where V is the membrane potential, I_{ext} is the external current, and C is the membrane capacitance. m and n are the fraction of open calcium and potassium channels, respectively. The ionic currents in (1) are defined as

$$\begin{aligned} &I_{\mathrm{L}} = g_{\mathrm{L}}(V - v_{\mathrm{L}}),\ I_{\mathrm{Ca}} = g_{\mathrm{Ca}}m(V - v_{\mathrm{Ca}}), \\ &I_{\mathrm{K}} = g_{\mathrm{K}}n(V - v_{\mathrm{K}}), \end{aligned} \tag{4}$$

where g_{L}, g_{Ca}, and g_{K} are the maximum conductances of the leak, calcium, and potassium channels, respectively. Also v_{L}, v_{Ca}, and v_{K} are the Nerst reversal potentials of the leak, Ca^{2+}, K^+ and Na^+ channels, respectively.

Taking into account the contribution of Na^+ on membrane depolarisation, we extend the ML model by adding Na^+ current, $I_{\mathrm{Na}} = g_{\mathrm{Na}}w(V - v_{\mathrm{Na}})$, in (1). With this current the ML model becomes a four-dimensional system of ODEs defined as

$$\mathrm{C}\frac{dV}{dt} = I_{\mathrm{ext}} - I_{\mathrm{L}} - I_{\mathrm{Ca}} - I_{\mathrm{K}} - I_{\mathrm{Na}}, \tag{5}$$

$$\frac{dm}{dt} = \lambda_m(V)(m_\infty(V) - m), \tag{6}$$

$$\frac{dn}{dt} = \lambda_n(V)(n_\infty(V) - n), \tag{7}$$

$$\frac{dw}{dt} = \lambda_w(V)(w_\infty(V) - w). \tag{8}$$

The equivalent circuit representation of the cell membrane with four ionic channels, I_{L}, I_{Ca}, I_{K}, and I_{Na}, is shown in Fig. 1.

The fraction of open Ca^{2+}, K^+ and Na^+ channels at steady state, denoted by m_∞, n_∞, and w_∞ are defined as

$$m_\infty(V) = 0.5\left(1 + \tanh\left(\frac{V - \bar{v}_1}{\bar{v}_2}\right)\right),$$

$$n_\infty(V) = 0.5\left(1 + \tanh\left(\frac{V - \bar{v}_3}{\bar{v}_4}\right)\right),$$

$$w_\infty(V) = 0.5\left(1 + \tanh\left(\frac{V - \bar{v}_5}{\bar{v}_6}\right)\right).$$

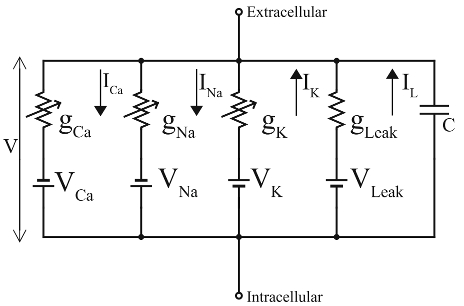

Fig. 1 Equivalent circuit representation of the cell membrane with four ionic channels

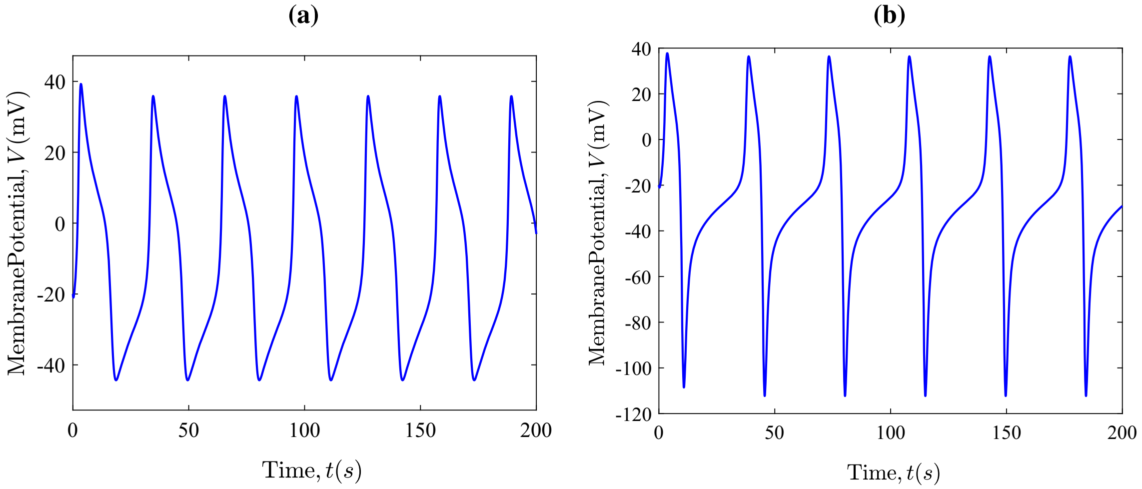

Fig. 2 Time series of the membrane potential V when the Na$^+$ conductance g$_{Na}$ is: **a** blocked ($g_{\text{Na}} = 0$); **b** unblocked ($g_{\text{Na}} \neq 0$)

The voltage-dependent rate constants associated with calcium, potassium and sodium channels are

$$\lambda_m(V) = \psi_m \cosh\left(\frac{V - \bar{v}_1}{2\bar{v}_2}\right),$$

$$\lambda_n(V) = \psi_n \cosh\left(\frac{V - \bar{v}_3}{2\bar{v}_4}\right),$$

$$\lambda_w(V) = \psi_w \cosh\left(\frac{V - \bar{v}_5}{2\bar{v}_6}\right),$$

Unless stated otherwise, parameter values are as listed in Gall and Zhou [14]: C = 1, $I_{\text{ext}} = 50$, $\text{g}_{\text{L}} = 2$, $v_{\text{L}} = -50$, $\text{g}_{\text{Ca}} = 4$, $v_{\text{Ca}} = 100$, $\text{g}_{\text{K}} = 8$, $v_K = -70$, $\text{g}_{\text{Na}} = 2$, $v_{\text{Na}} = 55$, $v_1 = -1$, $v_2 = 15$, $v_3 = 10$, $v_4 = 14.5$, $v_5 = 5$, $v_6 = 15$, $\psi_m = 1$, $\psi_n = 0.0667$, $\psi_w = 0.033$.

2.1 Changes to excitable dynamics as a parameter is varied

To analyse the model, we first assess the effects of Na$^+$ current on electrical activity. To do this, we block the conductance g_{Na} for the Na$^+$ current. The model is integrated numerically using the standard fourth-order Runge–Kutta method using a step size of 0.05 in the numerical software XPPAUT [8]. Figure 2a and b show the time series of the membrane potential V for model (5)–(8) when the Na$^+$ conductance is blocked and unblocked, respectively. Over a range of parameters considered, we found that the addition of Na$^+$ current causes the membrane potential to shift to more hyperpolarised values for hyperpolarised states, see Fig. 2b. This tells us that the effects of Na$^+$ conductance is non-negligible.

As seen in previous studies [11,16], variation of parameters can result in changes to dynamical behaviour of the model, for example, transitions from a rest state to periodic oscillations and vice versa. Here, we investigate the effects of maximum conductance on the dynamical behaviour of model (5)–(8). The dynamics of the membrane potential V upon varying Na$^+$ current conductance g_{Na} is shown in Fig. 3. For the range of values of g_{Na} considered, the system either converge to a rest state or oscillatory state. For extremely low values of g_{Na}, a single action potential is observed. In particular, the time evolution and its corresponding phase space for $g_{\text{Na}} = -20$ are shown in Fig. 3a and b, respectively. Upon increasing g_{Na}, periodic oscillations of action potentials are observed in the system, see Fig. 3c. The periodic oscillations correspond to a closed loop in the phase space, see Fig. 3d. The closed loop is also known as a limit cycle or periodic orbit. Further increasing g_{Na}, the system stabilises to a steady state, see Fig. 3e and f. Similar behaviours are observed when g_{K} and g_{Ca} are varied (results not shown). A detailed bifurcation analysis is given in Sect. 3 to further understand how the dynamical properties of model (5)–(8) change as parameter values is varied.

3 Numerical bifurcation analysis

With the aid of bifurcation analysis, we examine the dynamical behaviour of model (5)–(8) as different model parameters are varied in turn. The bifurcation diagrams are produced in XPPAUT and edited in MATLAB. The continuation parameters used in XPPAUT are `NTST=100`, `NMAX=2000`, `Method=stiff`, `EPSL=1e-7` , `EPSU=1e-7`, `EPSS=1e-7`, `ITMX=20`, `ITNW=20`, `DSMIN=1e-05`, `DSMAX=0.05`. The abbreviations and labels for the bifurcation points are given in Table 1.

3.1 Influence of g_{Na}

Here, we vary g_{Na} to explore the effects of Na$^+$ current on the dynamical behaviour of model (5)–(8). Figure 4 is a bifurcation diagram of the membrane

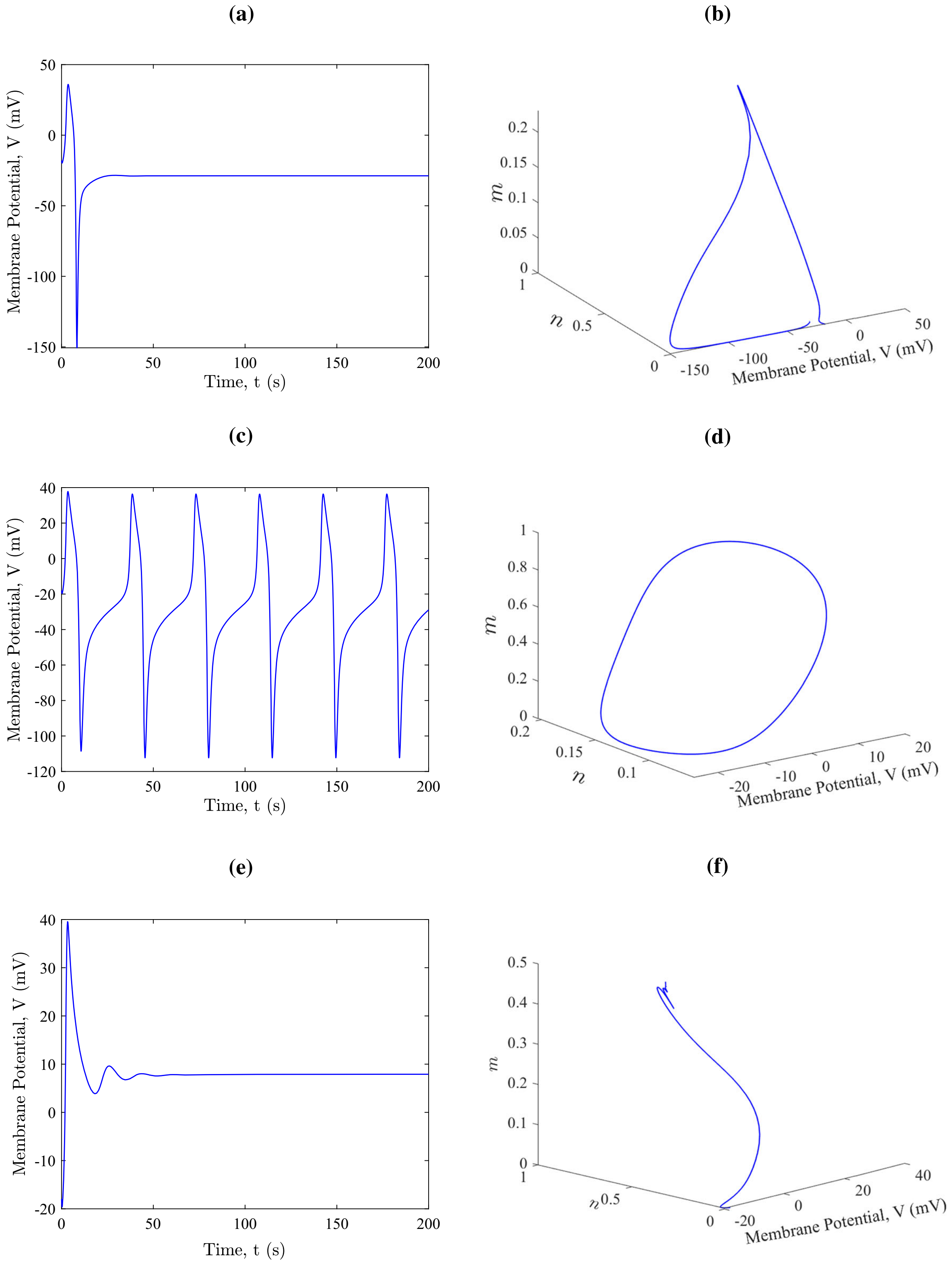

Fig. 3 Numerical simulations of the membrane potential V for **a** $g_{\mathrm{Na}} = -20$; **c** $g_{\mathrm{Na}} = -10$; **e** $g_{\mathrm{Na}} = 1.8$. Their corresponding phase space are (**b**), (**d**) and (**f**), respectively

Table 1 Abbreviations and notations of bifurcation points

Bifurcation	Abbreviation
Hopf bifurcation	HB
Saddle-node bifurcation	SN
Saddle-node bifurcation of cycles	SNC
Homoclinic bifurcation	HC
Period-doubling bifurcation	PD

potential V upon varying g_{Na} with other parameters fixed. For the range of values of g_{Na} considered, there exists a unique equilibrium. The system has a stable equilibrium except between two Hopf bifurcations where the equilibrium is unstable. As seen in Fig. 4a, the system loses stability through a subcritical Hopf bifurcation HB_1 at $g_{\mathrm{Na}} \approx -13.305$ and regains stability at another subcritical Hopf bifurcation HB_2 at $g_{\mathrm{Na}} \approx 0.69436$. The unstable limit cycle generated at HB_1 gain stability through a saddle-node bifurcation of cycle SNC_1 at $g_{\mathrm{Na}} \approx -13.4394$, and loses stability at a period-doubling bifurcation PD_1. The unstable limit cycle branch regains stability through another SNC_3 at $g_{\mathrm{Na}} \approx -13.1223$. The stable double-period limit cycle branch emanated from the PD_1 loses stability at another period-doubling bifurcation PD_2 at $g_{\mathrm{Na}} \approx -13.4323$, and it regains stability through a SNC_2 at $g_{\mathrm{Na}} \approx -13.2516$ before converging to the first unstable limit cycle branch at $g_{\mathrm{Na}} \approx -13.1223$, see Fig. 4b. Upon further increasing the value of g_{Na}, the limit cycle loses stability in a SNC_4 at $g_{\mathrm{Na}} \approx 1.10527$ before it ends in a HB point at $g_{\mathrm{Na}} \approx 0.69436$.

Continuation of PD_2 bifurcation results in another stable limit cycle that loses stability at a period doubling bifurcation PD_4, the period of this limit cycle is double the period of the limit cycle of PD_2. Continuing this process results in a cascade of PD bifurcations of limit cycles, and this may lead to chaotic dynamics in the system [27,40]. Table 2 shows the values and period of the period doubling bifurcations that arise as g_{Na} is varied. The projection of the periodic trajectories for

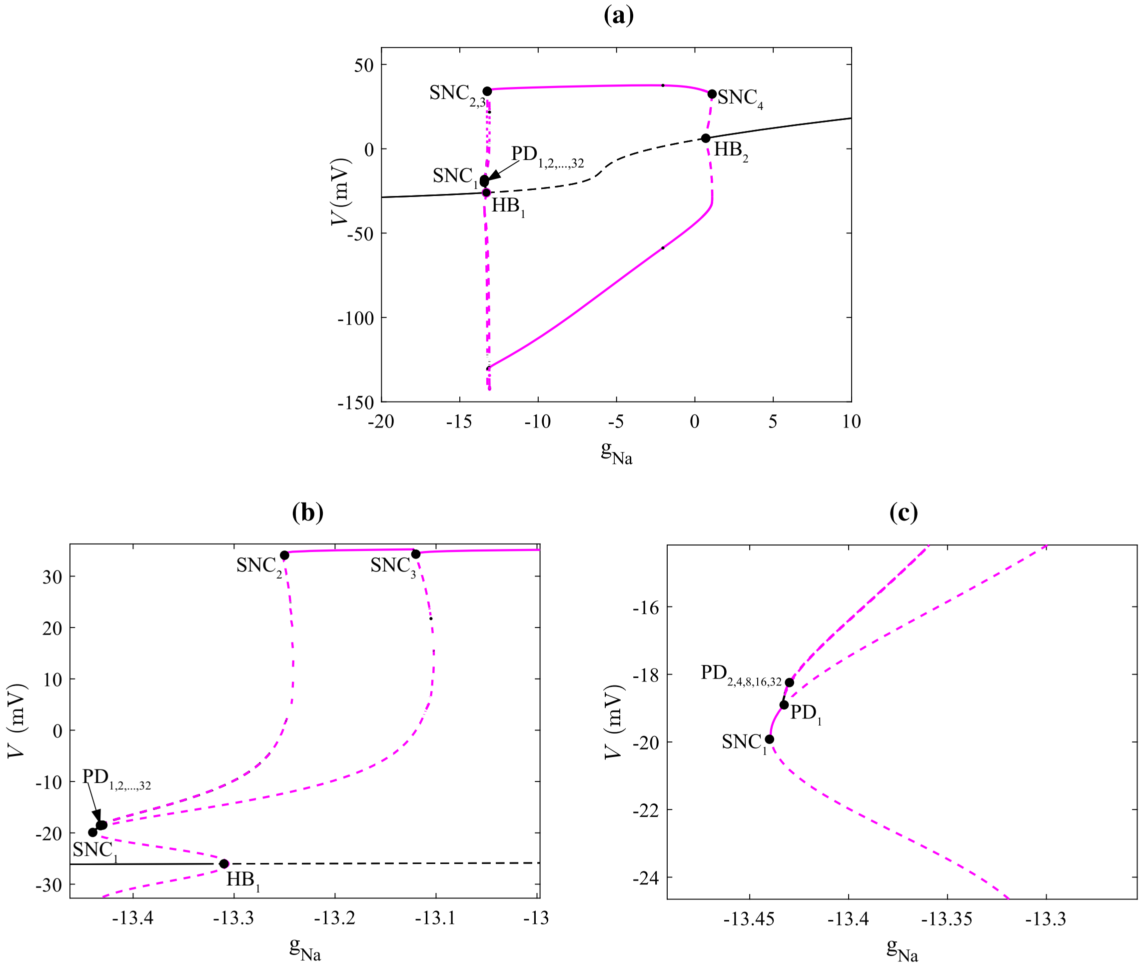

Fig. 4 **a** Bifurcation diagram of the membrane potential V with g_{Na} as bifurcation parameter. The remaining parameter values are fixed as in Sect. 2. **b**–**c** Are enlargements of (**a**). Continuous [dashed] curves correspond to stable [unstable] solutions. Black [mangenta] curves correspond to equilibria [periodic oscillations]. *HB* Hopf bifurcation, *SN* saddle-node bifurcation (of an equilibrium), *SNC* saddle-node bifurcation of a periodic orbit, *PD* period-doubling bifurcation

Table 2 Summary of the parameter values and period of Period doubling bifurcations that arise as g_{Na} is varied

Bifurcation	g_{Na}	Period
PD_1	−13.4334	36.0272
PD_2	−13.4323	72.1846
PD_4	−13.4321	144.489
PD_8	−13.4320	289.001
PD_{16}	−13.4320	578.025
PD_{32}	−13.4320	1156.05

Period-1, 2, 4, 8, 16 and 32 onto (V, n, m) phase space is illustrated in Fig. 5. All the double-period unstable limit cycles generated at each PD points undergo SNC bifurcations before they converge to the limit cycle emanated from the first HB bifurcation.

3.2 Influence of g_{K} and g_{Ca}

Figure 6a shows the bifurcation diagram of the membrane potential V as g_{K} is varied. For the values of g_{K} considered, there exists a unique equilibrium. For extremely low values and high values of g_{K}, the equilibrium is stable. Increasing g_{K}, the system loses stability through a subcritical Hopf bifurcation HB_1 at $g_{\mathrm{K}} \approx 10.029$ and this leads to emergence of an unstable limit cycle which becomes stable through a saddle node bifurcation of cycles SNC_1 at $g_{\mathrm{K}} \approx 9.345$. As g_{K} increases further, the stable limit cycle changes stability in another saddle node bifurcation of cycles SNC_2 at $g_{\mathrm{K}} \approx 46.598$. The unstable limit cycle ends in another subcritical Hopf bifurcation HB_2 at $g_{\mathrm{K}} \approx 42.583$. Bistability is observed, that is, a stable limit cycle coexists with a stable equilibrium when $9.345 \leq g_{\mathrm{K}} \leq 10.029$ and $42.583 \leq g_{\mathrm{K}} \leq 46.598$.

Next, we vary the value of the parameter g_{Ca}. Figure 6b shows the bifurcation diagram of the membrane potential V as g_{Ca} is varied. As g_{Ca} is varied, the system loses stability through a subcritical Hopf bifurcation HB_1 at $g_{\mathrm{Ca}} \approx 1.6191$ and this results in emergence of unstable limit cycle which becomes stable through a saddle node bifurcation of cycles SNC_1 at $g_{\mathrm{Ca}} \approx 1.5974$. As g_{Ca} increases further, the stable limit cycle loses stability in another saddle-node bifurcation SNC_2 at $g_{\mathrm{Ca}} \approx 3.2579$ and the unstable limit cycle ends in a subcritical Hopf bifurcation HB_2 at $g_{\mathrm{Ca}} \approx 2.8938$. Between the two subcritical Hopf bifurcations, there exists a unique unstable equilibrium point. For $1.5974 \leq g_{\mathrm{Ca}} \leq 1.6191$ and $2.8938 \leq g_{\mathrm{Ca}} \leq 3.2579$, a stable limit cycle coexists with a stable equilibrium and the system is bistable. For these values of g_{Ca}, a stable limit cycle coexists with a stable equilibrium.

3.3 Influence of I_{ext}

Apart from the maximum conductance of ionic channels, the influence of external current is highly important while investigating the dynamics of action potentials in electrophysiological studies. Here, we consider the effects of I_{ext} using two parameter sets. For set I, the parameter values are as listed in Sect. 2. Figure 7a is a bifurcation diagram of the membrane potential V with the applied current I_{ext} as a bifurcation parameter, other parameters fixed. For very low value of I_{ext}, a unique stable equilibrium point exists. Upon increasing I_{ext}, the system changes stability through a saddle node bifurcation SN_1 at $I_{\mathrm{ext}} \approx 30.52$ and the unstable branch fold back via another saddle node bifurcation SN_2 at $I_{\mathrm{ext}} \approx -39.57$. Between the two SN bifurcations, the system has three equilibria: one stable (lower branch) and two unstable (upper and middle branch), see Fig. 7a. The upper unstable branch changes stability at a subcritical Hopf bifurcation HB at $I_{\mathrm{ext}} \approx 6.656$ before the system returns to a rest state as I_{ext} increases. The unstable limit cycle emanated from HB fold back and changes to a stable limit cycle through a saddle node bifurcation of cycles SNC_1 at $\mathrm{I}_{\mathrm{ext}} \approx 26.84$. The limit cycle loses stability at another SNC_2 at $\mathrm{I}_{\mathrm{ext}} \approx 22.99$ before it terminates at $I_{ext} \approx 23.79$.

For set II, $v_6 = 3$ while other parameters are fixed as in Sect. 2. A bifurcation diagram of the membrane potential V with I_{ext} as bifurcation parameter is shown in Fig. 8a. For $I_{\mathrm{ext}} < -8.7715$, there exists a unique stable equilibrium point. Upon increasing I_{ext}, the system loses stability through a subcritical Hopf bifurcation HB_1 at $I_{\mathrm{ext}} \approx 33.29650$. The unstable limit cycle emanated from HB_1 ends in an homoclinic bifurcation HC_1 at $I_{\mathrm{ext}} \approx 33.2911$, see Fig. 8b. The curve of the homoclinic orbit is shown in Fig. 9a. Increasing I_{ext} slightly there appears a saddle-node bifurcation SN_1 at $I_{\mathrm{ext}} \approx 33.2026$, the unstable branch fold back at another saddle-node bifurcation SN_2 at $I_{\mathrm{ext}} \approx -8.7715$.

As I_{ext} increases further, the system passes through another saddle node bifurcation SN_3 at $I_{\mathrm{ext}} \approx 0.8353$. For $I_{\mathrm{ext}} \in [\mathrm{SN}_2, \mathrm{SN}_3]$, there exist three equilibria; one stable and two unstable. The branch of SN_3 bifurcation folds at another saddle-node bifurcation SN_4 at $I_{\mathrm{ext}} \approx -1.7961$, and the unstable upper branch becomes stable in another subcritical Hopf bifurcation HB_2. For $I_{\mathrm{ext}} \in [\mathrm{SN}_4, \mathrm{HB}_2]$, there exist five equilibria; one stable and four unstable equilibria. Also, for $I_{\mathrm{ext}} \in [\mathrm{HB}_2, \mathrm{SN}_3]$, there exist five equilibria; two stable and three unstable. For this parameter values, the system is bistable, that is, coexistence of two stable equilibria. To the right of SN_1, the system has a unique stable equilibrium.

The unstable limit cycle generated at the Hopf bifurcation HB_2 fold back at $I_{\mathrm{ext}} \approx 10.80$ and slightly after the fold point appears a period-doubling bifurcation PD_1 at $I_{\mathrm{ext}} \approx 10.77$. At PD_1, the limit cycle bifurcates into unstable double-period and unstable limit cycles, and they both end in an homoclinic bifurcation, see Fig. 8c. The curve of the homoclinic orbit is shown in Fig. 9b. Continuation from the period-doubling PD_1 results in period-doubling bifurcation PD_2, subsequently, the PD_2 results in period-doubling bifurcation PD_4. Table 3 shows the parameter values for the period-doubling and homoclinic bifurcations and their corresponding periods as I_{ext} is var-

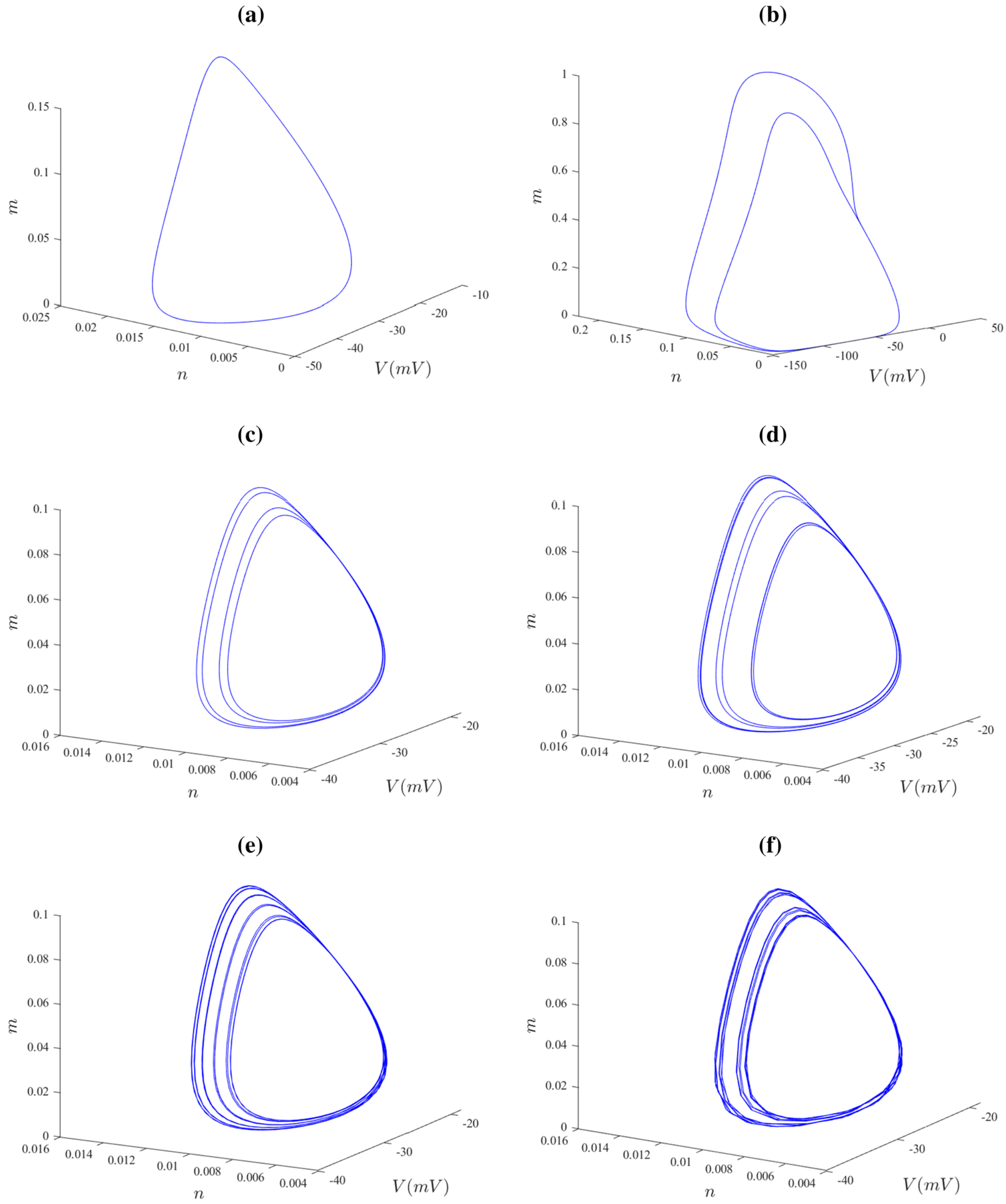

Fig. 5 Phase-space of (5)–(8) showing the cascade of period-doubling bifurcations. **a** Period-1, **b** Period-2, **c** Period-4, **d** Period-8, **e** Period-16, **f** Period-32, respectively

ied. The projections of periodic trajectories for period-1, 2, 4 onto (V, n, m) phase space are shown in Fig. 10.

3.4 Two parameter bifurcation analysis

In this section, we perform two parameter bifurcation analysis of (5)–(8) in $(I_{\text{ext}}, g_{\text{K}})$ plane. The bifurcation diagram shown in Fig. 13 is produced via numerical continuation software MATCONT [6]. The software implements Moore-Penrose continuation method to compute family and path of existing solution curves as parameters are varied. It is able to detect various kinds of bifurcations, switch to and compute the bifurcated branches, and allows us to follow the loci of the bifurcations in two parameters to detect codimension-2 bifurcation

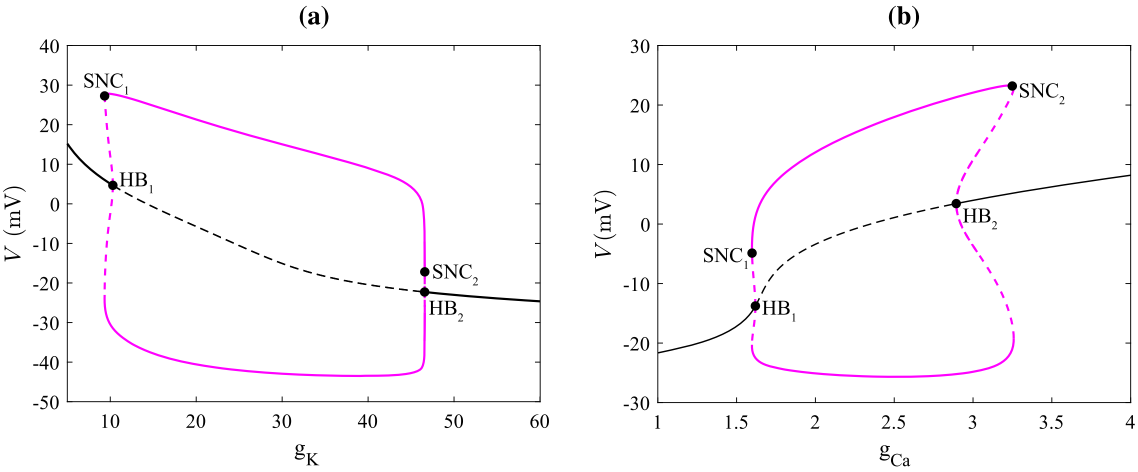

Fig. 6 Bifurcation diagrams of the membrane potential V with **a** g_{K}, **b** g_{Ca} as the bifurcation parameters and other parameters are fixed as in Sect. 2. The labels and other conventions are as in Fig. 4

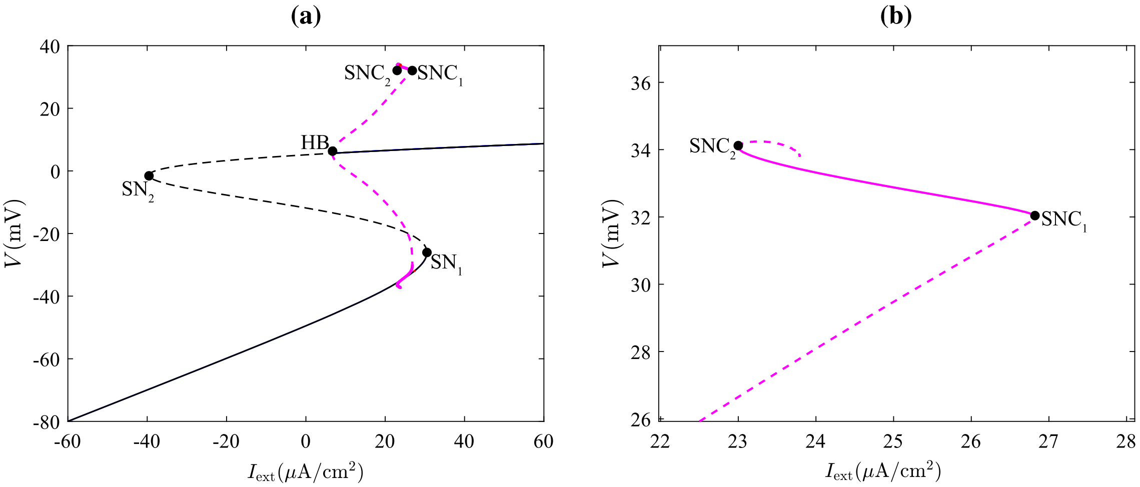

Fig. 7 **a** Bifurcation diagram of the membrane potential V with $\mathrm{I}_{\mathrm{ext}}$ as the bifurcation parameter and other parameters are fixed as in Sect. 2. The labels and other conventions are as in Fig. 4

points. The step-by-step procedures for generating the codimension-2 bifurcation diagram Fig. 13 in the GUI of MATCONT are given below:

i. First we integrate (5)–(8) from initial state variable values $(V, m, n, w) = (-20, 0, 0, 0)$ until the solution converges to an equilibrium point.
ii. Then we compute the equilibrium curve with I_{ext} as a continuation parameter. To initialise the equilibrium continuation from the last point in (i), we set $I_{\mathrm{ext}} = 50$, `ntst` $= 40$, and `ncol` $= 4$ in the **Starter** window and then compute **Forward** and **Backward**. Two Hopf bifurcations and four saddle-node bifurcations of equilibria are detected along the curve. The MATCONT window during the computation of the equilibrium curve is shown in Fig. 11.
iii. Next, we compute the limit cycles from the Hopf bifurcations. In the **Starter** window we set I_{ext} as bifurcation parameter and activate `period` to follow the period of oscillation along with the continuation. We compute **Forward** to start the continuation from the Hopf bifurcation in the lower branch, MATCONT detects no special point except that the unstable limit cycle that emanates from the Hopf bifurcation terminates at an homoclinic bifurcation, see Fig. 12a. Similarly, we compute **Forward** to start continuation from the Hopf bifurcation in the upper branch, an unstable limit cycle emanated from the Hopf bifurcation also terminated an homoclinci bifurcation and along the computation three period-doubling bifurcations are detected, see Fig. 12b.
iv. Finally, in the **Continuer** window we set `MaxStepSize` $= 1$ and select I_{ext} and g_{K} as bifurcation parameters in the **Starter** window. We then compute **Forward** and **Backward** at the Hopf bifurcation to produce the Hopf locus. Similarly, the loci of the saddle-node bifurcation and period-doubling bifurcation are initialised from each bifur-

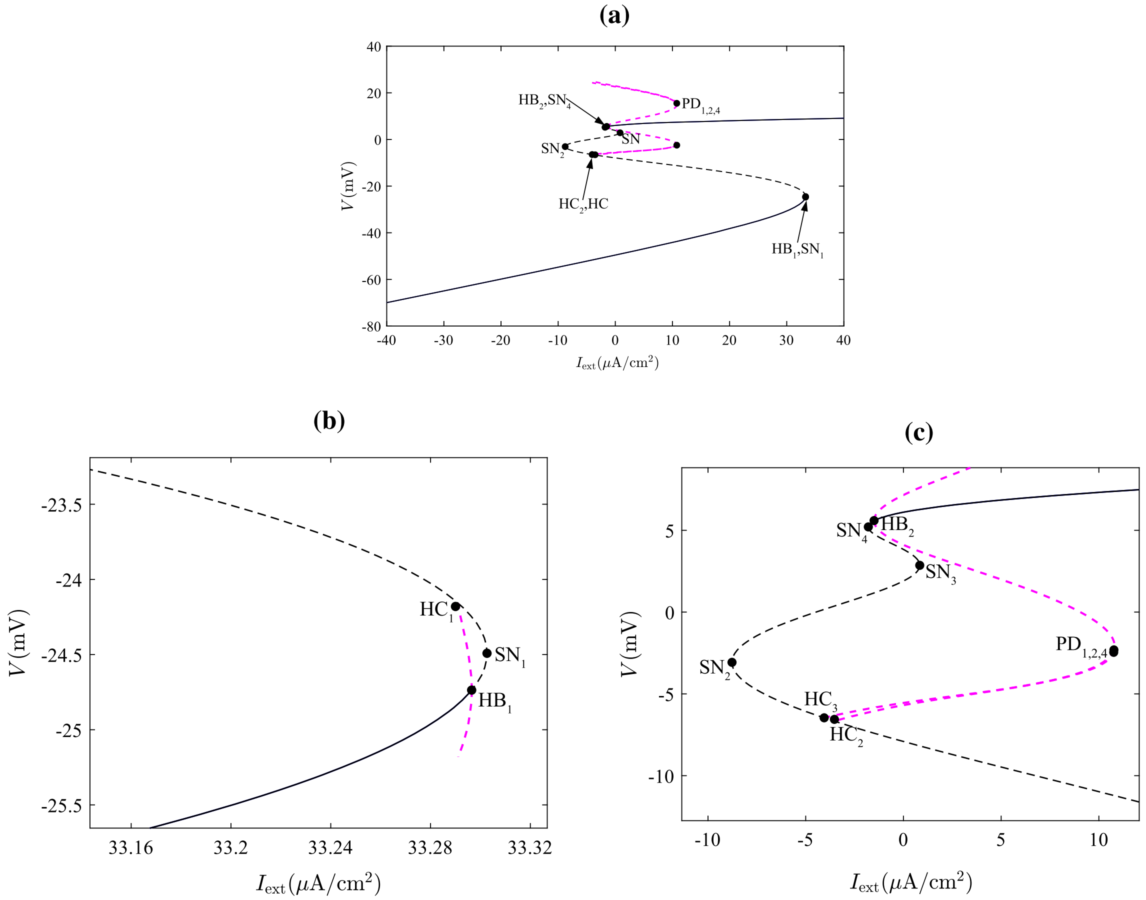

Fig. 8 **a** Bifurcation diagram of membrane potential V with I_{ext} as a bifurcation parameter. **b**–**c** Are enlargements of (**a**). and other parameters are fixed as in Sect. 2. The labels and other conventions are as in Fig. 4

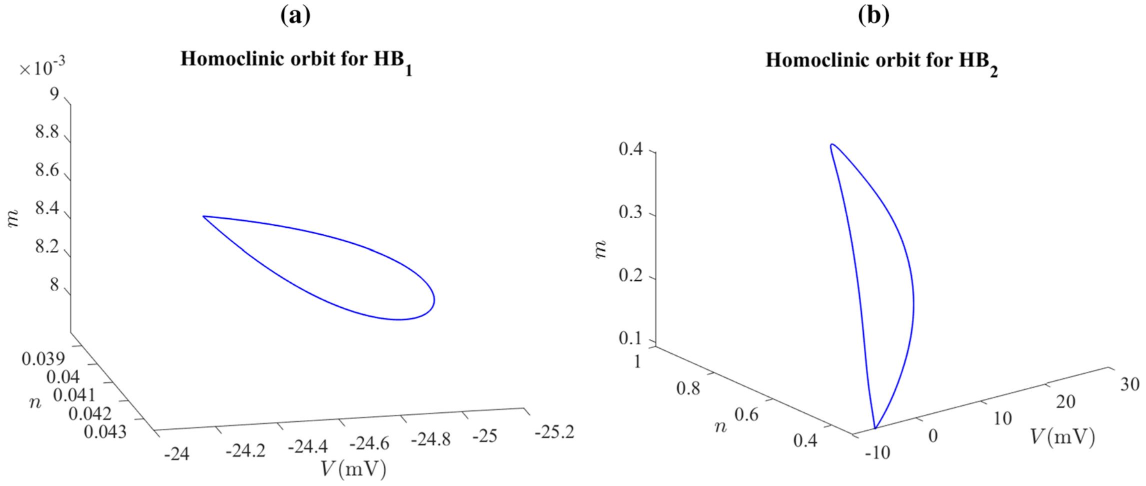

Fig. 9 The curves of homoclinic orbits of the periodic oscillation emanated at **a** HB$_1$; **b** HB$_2$

cation points, respectively. Several codimension-2 bifurcations are detected and their descriptions are explained in Table 4.

Figure 13 is divided into regions with respect to different types of dynamical behaviour and we have assigned each region a number, see Table 5. In the remainder of this section, we describe the dynamics of model (5)–(8) as I_{ext} and g_{K} are varied.

For sufficiently large values of g_{K}, there are two supercritical Hopf bifurcations HB$_1$ and HB$_2$. Thus for slice l_1 in Fig. 13 there are period solutions in region

Table 3 Summary of the parameter values and period of period doubling and homoclinic bifurcations that arise as I_{ext} is varied

Bifurcation point	I_{ext}	Period
PD_1	10.7705	33.5585
PD_2	10.7584	67.1396
PD_4	10.7555	134.353
HC_1	33.2911	$2.61499E{+}08$
HC_2	-4.05553	$3.95045E{+}09$

II. A codimension-1 bifurcation diagram along slice l_1 for which $g_{\text{K}} = 60$ is shown in Fig. 14a. The stable equilibrium solution loses stability through a Hopf bifurcation HB_2 as I_{ext} is varied. A stable limit cycle emanated from HB_2 ends in another Hopf bifurcation HB_1 before the equilibrium regains stability via HB_1. Here the system passes through regions I→II→I. As the value of g_{K} decreases, there appears a generalised Hopf bifurcation, denoted GH_1, on the Hopf bifurcation locus at $g_{\text{K}} \approx 43.9007$. This is a codimension-2 point where the HB locus changes from supercritical SupHB to subcritical SubHB [28]. Below the GH_1, there are two Hopf bifurcations, a subcriticcal and a supercritical. Figure 14b is a bifurcation diagram along slice l_2 in Fig. 13 for which $g_{\text{K}} = 26$. The system passes through regions I→II→I as in the previous case (slice l_1) except that the stable equilibrium solution in region I loses stability through a subcritical Hopf bifurcation HB_2. An unstable limit cycle emanated from HB_2 changes stability via a saddle-node bifurcation of limit cycles (SNC), the stable limit cycle ends in a supercritical Hopf bifurcation HB_1 then to the left of HB_1 the equilibrium solution regains stability.

Upon further decrease in the value of g_{K}, the loci of saddle-node bifurcations SN_1 and SN_2 collide and annihilate in a cusp bifurcation CP_1 at $g_{\text{K}} \approx 18.1715$. As g_{K} decreases, a 1:2 resonance bifurcation R2 and two generalised period-doubling bifurcations GPD_1 and GPD_2 appear on the locus of period doubling bifurcation at $g_{\text{K}} \approx 12.624$, 15.982, and 13.535, respectively. Also, the loci of saddle-node bifurcations SN_3 and SN_4 collide and annihilate in a cusp bifurcation CP_3 at $g_{\text{K}} \approx 8.6962$ and the supercritical Hopf bifurcation SupHB changes to subcritical Hopf bifurcation in another generalised Hopf bifurcation GH_2 at $g_{\text{K}} \approx 11.3037$, see Fig. 15a.

As the value of g_{K} is decreased below CP_3, there exist four saddle-node bifurcations SN_1, SN_2, SN_3 and SN_4, an example is shown in Fig. 15b along slice l_3.

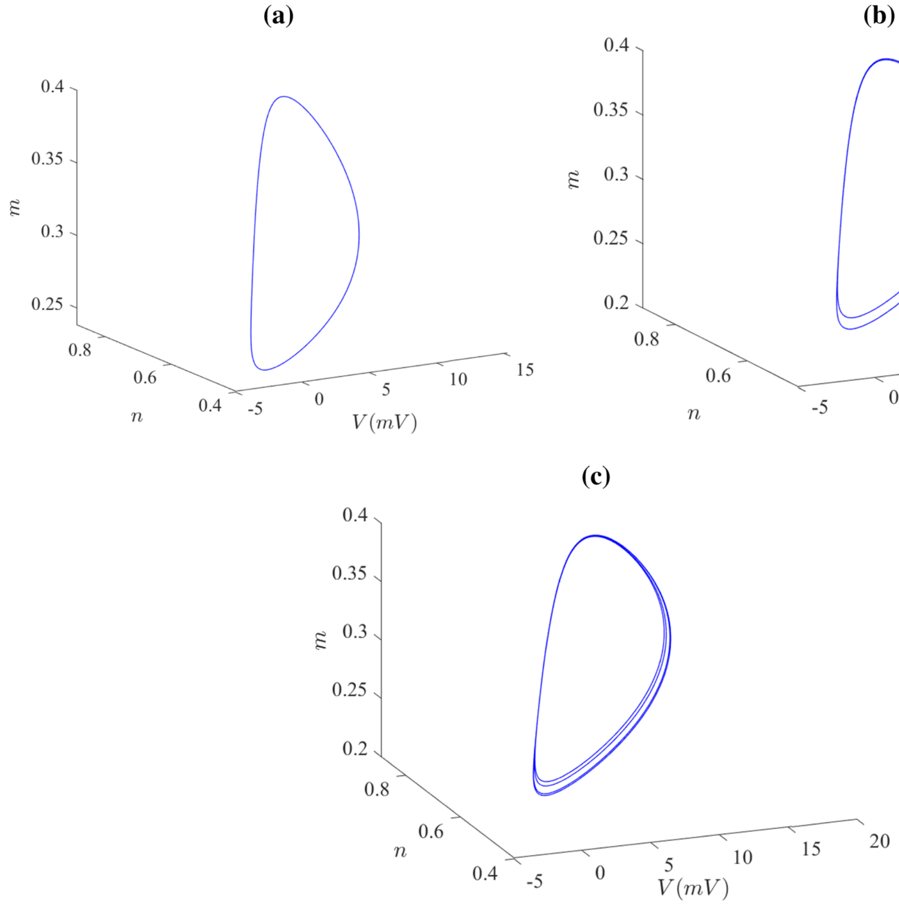

Fig. 10 Phase-space of (5)–(8) showing the period-doubling bifurcations in response to variation of I_{ext}. **a** Period-1, **b** Period-2 and **c** Period-4, respectively

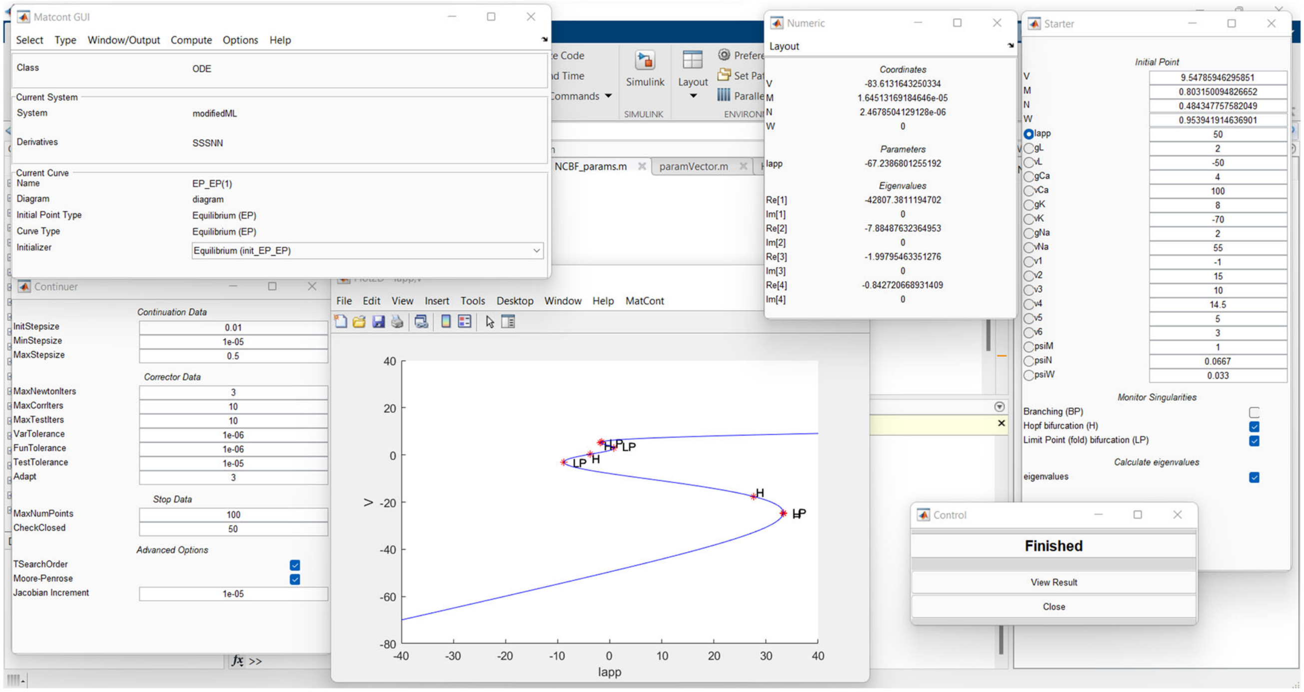

Class	ODE
Current System	
System	modifiedML
Derivatives	SSSNN
Current Curve	
Name	EP_EP(1)
Diagram	diagram
Initial Point Type	Equilibrium (EP)
Curve Type	Equilibrium (EP)
Initializer	Equilibrium (init_EP_EP)

Continuation Data	
InitStepsize	0.01
MinStepsize	1e-05
MaxStepsize	0.5
Corrector Data	
MaxNewtonIters	3
MaxCorrIters	10
MaxTestIters	10
VarTolerance	1e-06
FunTolerance	1e-06
TestTolerance	1e-05
Adapt	3
Stop Data	
MaxNumPoints	100
CheckClosed	50
Advanced Options	
TSearchOrder	☑
Moore-Penrose	☑
Jacobian Increment	1e-05

Coordinates	
V	-83.6131643250334
M	1.64513169184646e-05
N	2.4678504129128e-06
W	0
Parameters	
Iapp	-67.2386801255192
Eigenvalues	
Re[1]	-42807.3811194702
Im[1]	0
Re[2]	-7.88487632364953
Im[2]	0
Re[3]	-1.99795463351276
Im[3]	0
Re[4]	-0.842720668931409
Im[4]	0

Initial Point	
V	9.54785946295851
M	0.803150094826652
N	0.484347757582049
W	0.953941914636901
● Iapp	50
○ gL	2
○ vL	-50
○ gCa	4
○ vCa	100
○ gK	8
○ vK	-70
○ gNa	2
○ vNa	55
○ v1	-1
○ v2	15
○ v3	10
○ v4	14.5
○ v5	5
○ v6	3
○ psiM	1
○ psiN	0.0667
○ psiW	0.033
Monitor Singularities	
Branching (BP)	☐
Hopf bifurcation (H)	☑
Limit Point (fold) bifurcation (LP)	☑
Calculate eigenvalues	
eigenvalues	☑

Finished

Fig. 11 MATCONT window during the computation of the equilibrium curve

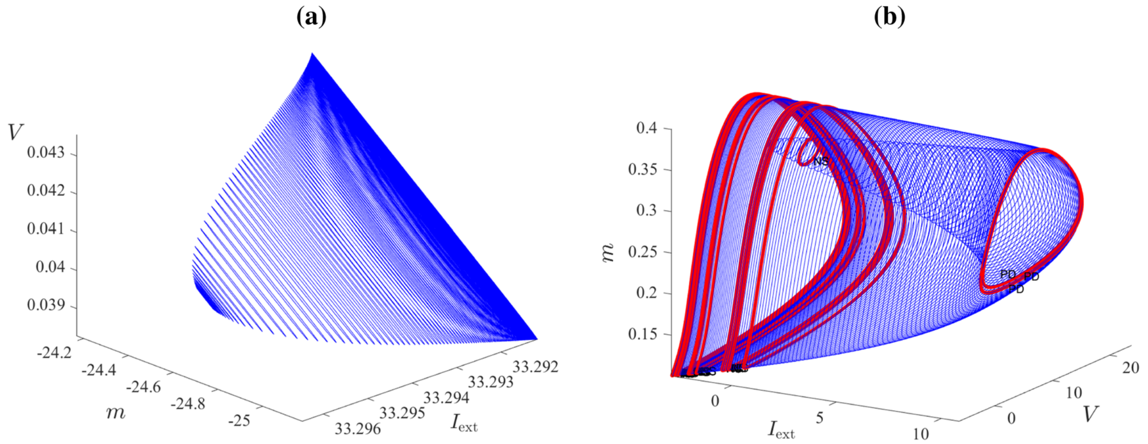

Fig. 12 A plot of the limit cycle that emanates from **a** the Hopf bifurcation in the lower branch; **b** the Hopf bifurcation in the upper branch of the equilibrium curve shown in Fig. 11

Table 4 Abbreviations of codimension-two bifurcations

Bifurcation	Abbreviation
Cusp bifurcation	$\mathrm{CP}_i\ i = 1, 2, 3$
Bogdanov-takens bifurcation	$\mathrm{BT}_i i = 1, 2$
Generalized Hopf bifurcation	$\mathrm{GH}_i\ i = 1, 2, 3$
Zero-Hopf bifurcation	ZH
Generalised period doubling bifurcation	$\mathrm{GPD}_i\ i = 1, 2$
1:2 Resonance	R2
Flip-flop bifurcation	LPPD

The corresponding codimension-1 bifurcation diagram for which $g_\mathrm{K} = 8$ is shown in Fig. 8a and described in Sect. 3.3. The system passes through regions I → III → V → VI → IV → I in Fig. 13. The loci of saddle-node bifurcations SN_2 and SN_3 collide and annihilate in a cusp bifurcation CP_2 at $g_\mathrm{K} \approx 18.1715$. As we decrease the value of g_K further, Bogdanov-Takens BT_1 and BT_2 occcur on the loci of saddle-nodes SN_2 and SN_1 at $g_\mathrm{K} \approx 7.1062$ and $g_\mathrm{K} \approx 6.9935$, respectively. The loci of subcritical Hopf bifurcations emanate from these codimension-2 points. These loci are tangential to SN_2 and SN_1 at these codimension-2 points. Observe also are zero-Hopf bifurcation ZH at $g_\mathrm{K} \approx 6.4099$, a codimension-2 where the locus of HB_2 intersect the locus of SN_4, and flip-flop bifurcation at $g_\mathrm{K} \approx 6.8379$ on the locus of period doubling bifurcation as g_K decreases.

Finally, as g_K is decreased further a generalised Hopf bifurcation, denoted GH_3, occurs on the Hopf bifurca-

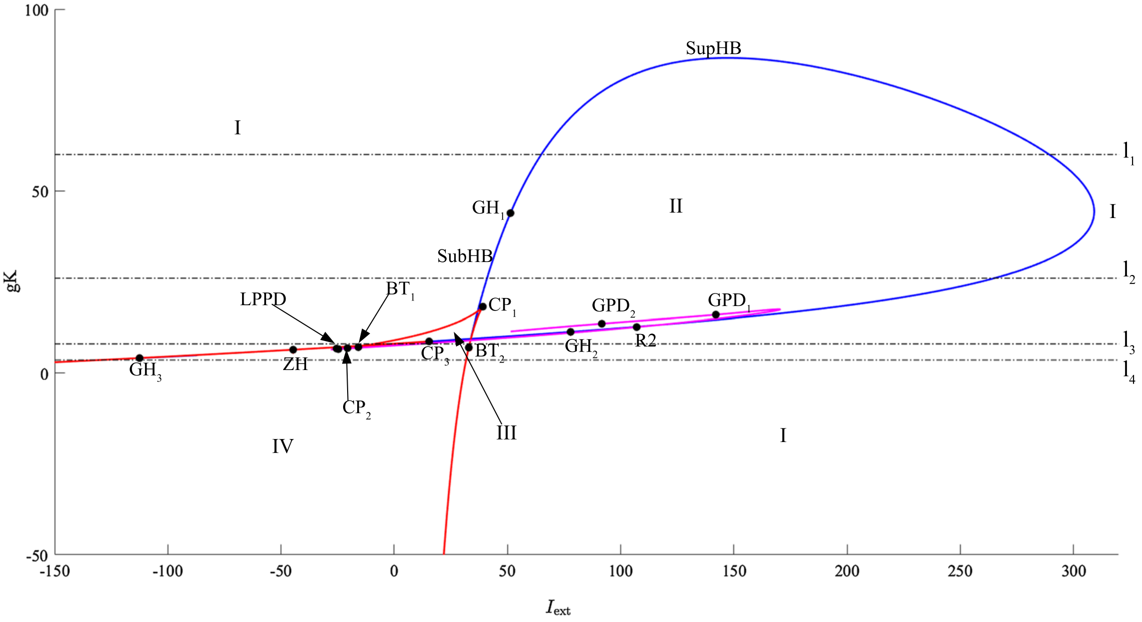

Fig. 13 Two parameter bifurcation diagram of (5)–(8) in the $(I_{\mathrm{ext}}, g_{\mathrm{K}})$-plane for parameter set II in Sect. 3.3 and other parameter values as in Sect. 2. The values of g_{K} in l_1, l_2, l_3, l_4 are 60, 26, 8 and 3.5, respectively. The blue, red and magenta curves are the loci of Hopf bifurcation, saddle-node bifurcation, and period doubling bifurcation. The labels for the codimension-2 bifurcations are explained in Table 4. The invariant sets that exist in each region are listed in Table 5

Table 5 Summary of the six different combinations of equilibria and limit cycles that arise in Fig. 13 and its magnifications, Figs. 15a, 15b, and 16a

Region	Existence of equilibria and limit cycles
I	One stable equilibrium, no limit cycles (rest state)
II	One unstable equilibrium, one stable limit cycle
III	One stable equilibrium, two unstable equilibria, no limit cycles
IV	Two stable equilibria, one unstable equilibrium, no limit cycles
V	One stable equilibrium, four unstable equilibria, one unstable limit cycle
VI	Two stable equilibria, three unstable equilibria, one unstable limit cycle

tion locus HB_2 at $g_{\mathrm{K}} \approx 4.1025$. Below this codimension-2 point, the only bifurcations that remain are the two saddle-node bifurcations SN_1 and SN_2. An example is shown Fig. 16a which is an enlargement of Fig. 13. A bifurcation diagram along slice l_4 for which $g_{\mathrm{K}} = 3.5$ is shown in Fig. 16b. Here the system passes through regions I → IV → I.

4 Conclusion

In this present paper, we have studied a 4D-ML model to explore the influence of second inward Na^+ currents on electrical activities of excitable tissues. This work is motivated by the results in [45], where it is reported that voltage-gated Na^+ currents appear to contribute to the depolarising stage of action potentials in some excitable cells. We focused on addressing the influence of maximum conductances of ion channels on the dynamics of the membrane potential. Upon varying the conductance associated with the Na^+ currents, g_{Na}, the model exhibits different electrical activities.

With the aid of numerical bifurcation analysis, we examined the effects of parameters on the dynamical behaviour of the model. Our results showed that increasing the maximum conductance of sodium current g_{Na}, the model transitions from rest state to periodic oscillations. For some values of g_{Na}, the model shows complex behaviour, specifically, it undergoes cascades of period-doubling bifurcations. It was found that the bifurcation structure of varying the maximum conductance of potassium current g_{K} is qualitatively similar to that of varying the maximum conductance of calcium current g_{Ca} except in reverse. That is, increasing the value of g_{K} results in the same qualitative changes to the dynamics of the model as decreasing the value of g_{Ca}.

We also showed qualitatively the effect of varying the external current I_{ext} on the dynamical behaviour of the model. Similar bifurcation diagram has been observed by Gall and Zhou [14], they discussed the bifurcation diagram in some detail, although without an explicit determination of the period oscillations thus their bifurcation diagram seems incomplete. However, in this work, we give a detailed bifurcation structure. We showed that the unstable periodic oscillations

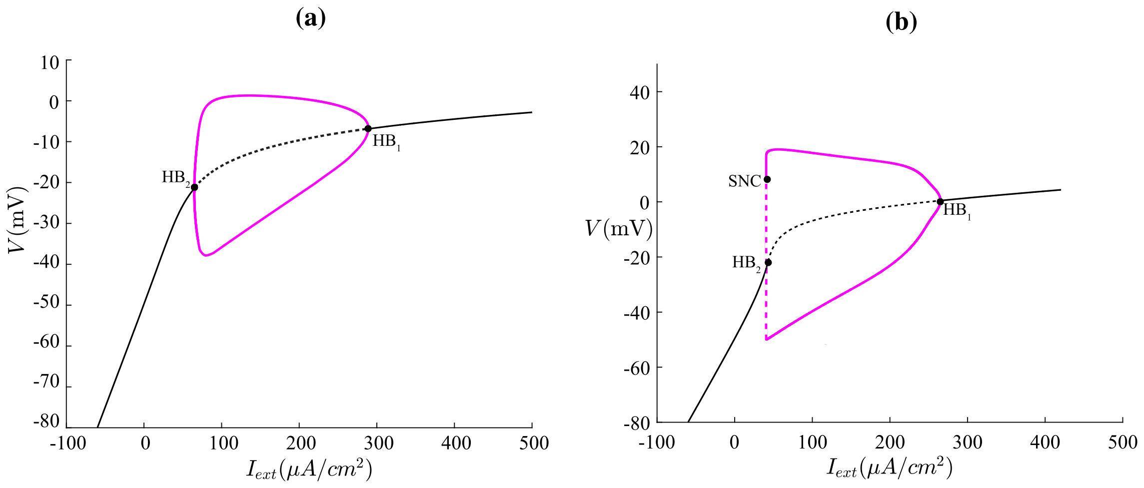

Fig. 14 **a** A codimension-1 bifurcation diagram along line l_1 with $g_K = 60$. **b** A codimension-1 bifurcation diagram along line l_2 with $g_K = 26$. The labels and other conventions are as in Fig. 4

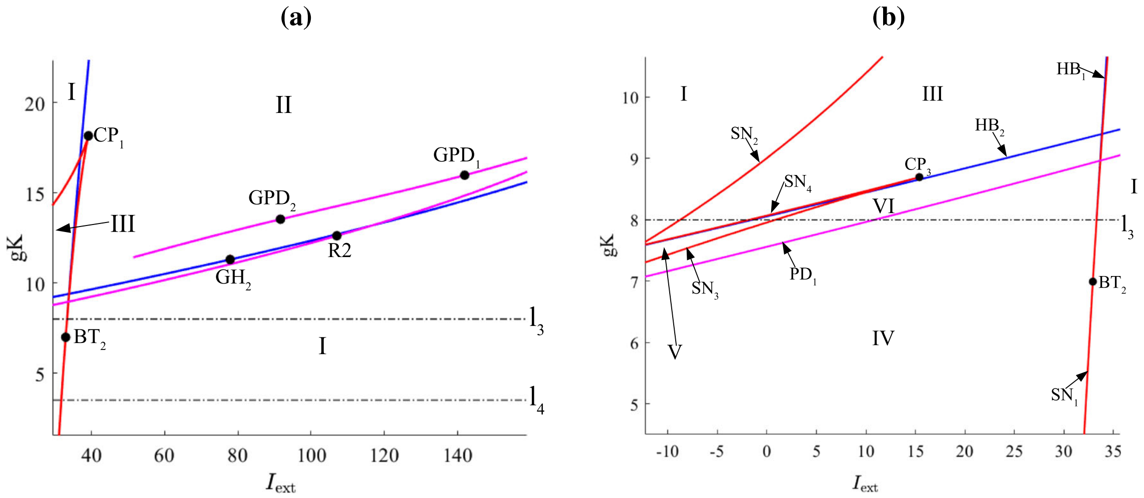

Fig. 15 **a** An enlargement of Fig. 13. **b** An enlargement of Fig. 13 showing line l_3 with $g_K = 8$. The labels and other conventions are as in Fig. 13 and Table 4

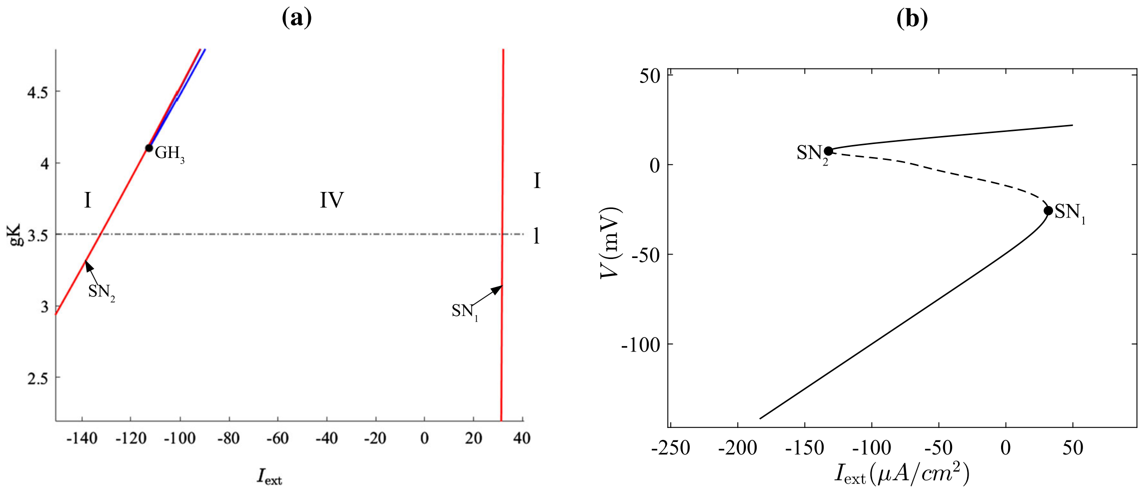

Fig. 16 **a** An enlargement of Fig. 13 showing lines l_4. **b** A codimension-1 bifurcation diagram along line with $g_K = 3.5$. The labels and other conventions are as in Fig. 13 and Table 4

emanated from the two Hopf bifurcations terminate in homoclinic bifurcations. We also observed cascades of period-doubling PD bifurcations for some values of I_{ext}. The existence of PD bifurcations is an indicator that the model can exhibit chaotic behaviour in some parameter regime.

The codimension-2 bifurcation analysis in $(I_{\text{ext}}, g_{\text{K}})$-plane gives further details on transitions between different electrical activities in the model. The electrical activities in the original ML model can be of Type I or II excitability depending on how the cell transitions from rest state to periodic oscillations is through a Hopf bifurcation. [11,44]. In Type I excitability, the cell transitions from rest to an oscillatory state via a saddle-node on an invariant circle bifurcation and in Type II excitability the transition is via a Hopf bifurcation. In this work, the model exhibits only Type II excitability.

The results in this paper showed that the Na^+ channels may influence the depolarisation stage of an action potential. It is hope that this model provides a framework that can aid in the understanding of various electrical activities in excitable cells. Based on the results of the present paper more complex behaviour is expected when two or more cells are coupled together, thus the dynamics of a network of cells would be addressed in future. The individual systems can be interconnected via ring-star network [35] , two-dimensional lattice [41], multilayer network [42] to account for various other spatio temporal patterns, chimera states.

Acknowledgments The authors are grateful for the extensive and constructive comments from the anonymous reviewers. SSM acknowledges Dr. Astero Provata for providing feedback, discussions on the manuscript and the School of Fundamental Sciences doctoral bursary funding during this research.

Author contributions

The presented idea was conceived by HOF. He wrote the MATCONT and XPPAUT codes. HOF and SSM carried out the numerical simulations and generated the figures. AA aided in the interpretation of the results. All authors jointly prepared the manuscript.

Data Availability Statement This manuscript has no associated data or the data will not be deposited. [Authors' comment: The XPPAUT and MATCONT code in this study are available from the corresponding author upon reasonable request.]

Declarations

Conflict of interest The authors declare that they have no conflict of interest.

References

1. T. Azizi, B. Alali, Impact of chloride channel on spiking patterns of Morris-Lecar model. Appl. Math. **11**, 650–669 (2020)
2. T. Azizi, R. Mugabi, The phenomenon of neural bursting and spiking in neurons: Morris-Lecar model. Appl. Math. **11**, 203–226 (2020)
3. B. Bao, Q. Yang, L. Zhu, H. Bao, Q. Xu, Y. Yu, M. Chen, Chaotic bursting dynamics and coexisting multistable firing patterns in 3D autonomous Morris-Lecar model and microcontroller-based validations. Int. J. Bifurc. Chaos **29**, 1950134 (2019)
4. R. Berra-Romani, M.P. Blaustein, D.R. Matteson, TTX-sensitive voltage-gated Na^+ channels are expressed in mesenteric artery smooth muscle cells. Am. J. Physiol. Heart Circ. Physiol. **289**, H137–H145 (2005)
5. T.R. Chay, Chaos in a three-variable model of an excitable cell. Phys. D Nonlinear Phenom. **16**(2), 233–242 (1985)
6. A. Dhooge, W. Govaerts, Y.A. Kuznetsov, MATCONT: a MATLAB package for numerical bifurcation analysis of ODEs. ACM Trans. Math. Soft. **29**, 141–164 (2003)
7. L. Duan, D. Zhai, X. Tang, Q. Lu, Bursting and mode transitions in coupled nonidentical modified morris-lecar neurons. In: *2010 International Workshop on Chaos-Fractal Theories and Applications*, pp. 293–296 (2010)
8. B. Ermentrout, *Simulating, Analyzing, and Animating Dynamical Systems: A Guide to XPPAUT for Researchers and Students* (SIAM Press, Philadelphia, 2002)
9. B. Ermentrout, D. Terman, *Foundations of Mathematical Neuroscience* (Springer, New York, 2008)
10. H. Fatoyinbo, *Pattern Formation in Electrically Coupled Pacemaker Cells*. PhD thesis, Massey University, Manawat, New Zealand (2020)
11. H.O. Fatoyinbo, R.G. Brown, D.J.W. Simpson, B. van Brunt, Numerical bifurcation analysis of pacemaker dynamics in a model of smooth muscle cells. Bull Math Bio **82**(95), 1–22 (2020)
12. R. FitzHugh, Impulses and physiological states in theoretical model of nerve membrane. Biophys. J. **1**, 445–466 (1961)
13. H. Fujii, I. Tsuda, Neocortical gap junction-coupled interneuron systems may induce chaotic behaviour itinerant among quasi-attractors exhibiting transient synchrony. Neurocomputing **58–60**, 151–157 (2004)
14. W. Gall, Y. Zhou, Including a second inward conductance in Morris and Lecar dynamics. Neurocomputing **26–27**, 131–136 (1999)
15. J.M. Gonzalez-Fernandez, B. Ermentrout, On the origin and dynamics of the vasomotion of small arteries. Math. Biosci. **119**, 127–167 (1994)
16. J.M. González-Miranda, Pacemaker dynamics in the full Morris-Lecar model. Commun. Nonlinear Sci. Numer. Simul. **19**, 3229–3241 (2014)
17. A. Gottschalk, P. Haney, Computational aspects of anesthetic action in simple neural models. Anesthesiology **98**, 548–564 (2003)
18. W. Govaerts, B. Sautois, The onset and extinction of neural spiking: a numerical bifurcation approach. J. Comput. Neurosci. **18**(3), 265–274 (2005)

19. H. Hartle, R. Wackerbauer, Transient chaos and associated system-intrinsic switching of spacetime patterns in two synaptically coupled layers of Morris-Lecar neurons. Phys. Rev. E **96**, 032223 (2017)
20. A.L. Hodgkin, A.F. Huxley, A quantitative description of membrane current and its application to conduction and excitation in nerve. J. Physiol. **117**(4), 500–544 (1952)
21. K.J. Iremonger, A.E. Herbison, Initiation and propagation of action potentials in gonadotropin-releasing hormone neuron dendrites. J. Neurosci. **32**(1), 151–158 (2020)
22. E.M. Izhikevich, *Dynamical Systems in Neuroscience: The Geometry of Excitability and Bursting* (MIT Press, Cambridge, 2007)
23. B. Jia, Negative feedback mediated by fast Inhibitory autapse enhances neuronal oscillations near a Hopf bifurcation point. Int. J. Bifurc. Chaos **28**(2), 1850030 (2018)
24. T. Jo, T. Nagata, H. Iida, H. Imuta, K. Iwasawa, J. Ma, K. Hara, M. Omata, R. Nagai, H. Takizawa, T. Nagase, T. Nakajima, Voltage-gated sodium channel expressed in cultured human smooth muscle cells: involvement of SCN9A. FEBS Lett. **567**(2–3), 339–343 (2004)
25. J. Keener, J. Sneyd, *Mathematical Physiology, Interdisciplinary Applied Mathematics*, vol. 8/1 (Springer, New York, 2009)
26. R.D. Keynes, E. Rojas, R.E. Taylor, J.L. Vergara, Calcium and potassium systems of a giant barnacle muscle fibre under membrane potential control. J. Physiol. **229**, 409–455 (1973)
27. P. Kügler, M. Bulelzai, A. Erhardt, Period doubling cascades of limit cycles in cardiac action potential models as precursors to chaotic early Afterdepolarizations. BMC Syst. Biol. **11**(42), 1–13 (2017)
28. Y.A. Kuznetsov, *Elements of Applied Bifurcation Theory*, 3rd edn. (Springer, New York, 1995)
29. J. Lafranceschina, R. Wackerbauer, Impact of weak excitatory synapses on chaotic transients in a diffusively coupled Morris-Lecar neuronal network. Chaos **25**, 013119 (2014)
30. M. Lv, J. Wang, G. Ren, J. Ma, X. Song, Model of electrical activity in a neuron under magnetic flow effect. Nonlinear Dyn. **85**, 1479–1490 (2016)
31. A.C. Marreiros, S.J. Kiebel, J. Daunizeau, L.M. Harrison, K.J. Friston, Population dynamics under the laplace assumption. Neuroimage **44**, 701–714 (2009)
32. S.R. Meier, J.L. Lancaster, J.M. Starobin, Bursting regimes in a reaction-diffusion system with action potential-dependent equilibrium. PLoS One **10**(3), 1–25 (2015)
33. A. Mondal, R.K. Upadhyay, J. Ma, B.K. Yadav, S.K. Sharma, Bifurcation analysis and diverse firing activities of a modified excitable neuron model. Cogn. Neurodyn. **13**(4), 393–407 (2019)
34. C. Morris, H. Lecar, Voltage oscillations in the barnacle giant muscle fiber. Biophys. J. **35**, 193–213 (1981)
35. S.S. Muni, A. Provata, Chimera states in ring-star network of Chua circuits. Nonlinear Dyn. **101**, 2509–2521 (2020)
36. J. Nagumo, S. Arimoto, S. Yoshizawa, An active pulse transmission line simulating nerve axon. Proc. IRE **50**(10), 2061–2070 (1962)
37. S.A. Prescott, S. Ratté, Y. De Koninck, T.J. Sejnowski, Nonlinear interaction between shunting and adaptation controls a switch between integration and coincidence detection in pyramidal neurons. J. Neurosci. **11**(36), 9084–9097 (2006)
38. S.A. Prescott, Y. De Koninck, T.J. Sejnowski, Biophysical basis for three distinct dynamical mechanisms of action potential initiation. PLoS Comput. Biol. **4**, 1000198 (2008)
39. K. Rajagopal, I. Moroz, B. Ramakrishnan, A. Karthikeyn, P. Duraisamy, Modified Morris-Lecar neuron model: effects of very low frequency electric fields and of magnetic fields on the local and network dynamics of an excitable media. Nonlinear Dyn. **104**, 4427–4443 (2021)
40. R. Seydel, *Practical Bifurcation and Stability Analysis*, vol. 5 (Springer, New York, 2010)
41. I.A. Shepelev, A.V. Bukh, S.S. Muni, V. Anishchenko, Role of solitary states in forming spatiotemporal patterns in a 2D lattice of van der pol oscillators. Chaos Soliton. Fract. **135**, 109725 (2020)
42. I.A. Shepelev, S.S. Muni, T.E. Vadivasova, Synchronization of wave structures in a heterogeneous multiplex network of 2D lattices with attractive and repulsive intra-layer coupling. Chaos **31**, 021104 (2021)
43. P. Smolen, J. Keizer, Slow voltage inactivation of Ca^{2+} currents and bursting mechanisms for the mouse pancreatic β-cell. J. Membrane Biol. **127**, 9–19 (1992)
44. K. Tsumoto, H. Kitajima, T. Yoshinaga, K. Aihara, H. Kawakami, Bifurcations in Morris-Lecar neuron model. Neurocomputing **69**(4–6), 293–316 (2006)
45. A.V. Ulyanova, R.E. Shirokov, Voltage-dependent inward currents in smooth muscle cells of skeletal muscle arterioles. PLoS One **13**(4), e0194980 (2018)
46. R.K. Upadhyay, A. Mondal, W.W. Teka, Mixed mode oscillations and synchronous activity in noise induced modified Morris-Lecar neural system. Int. J. Bifurc. Chaos **27**, 1730019 (2017)
47. H. Wang, L. Wang, L. Yu, Y. Chen, Response of Morris-Lecar neurons to various stimuli. Phys. Rev. E **83**, 021915 (2011)
48. F. Zeldenrust, P.J.P. Chameau, W.J. Wadman, Reliability of spike and burst firing in thalamocortical relay cells. J. Comput. Neurosci. **35**, 317–334 (2013)
49. Z. Zhao, H. Gu, Transitions between classes of neuronal excitability and bifurcations induced by autapse. Sci. Rep. **7**(1), 6760 (2017)